Robust Higher Order Control Barrier Functions for Shared Control and Vehicle Safety

James Dallas, John Talbot, *Member, IEEE*, Makoto Suminaka, Illés Vörös, Gábor Orosz, *Senior Member, IEEE*, and John Subosits

***Abstract*—This article develops a control barrier function (CBF)-based approach to mitigate a vehicle from losing control and entering the unrecoverable part of the state space. The maximal phase recoverable ellipse (MPREl) is constructed in the sideslip angle–yaw rate phase plane, defining a safe set where the vehicle remains in a recoverable state, and an exponential CBF (ECBF) is developed based on this set. The approach accounts for uncertainty, yielding a novel robust adaptive higher order CBF (HOCBF) that remains control affine. A quadratic program is formulated to filter the driver's commands in a minimally invasive fashion in a shared control setting. The approach is validated both via simulations and on an experimental vehicle, demonstrating safe operation under dynamic uncertainty in a shared control setting when drifting, that is, operating in the open-loop unstable regime where the rear tires are sliding. Finally, the approach achieves safe operation in a computationally efficient manner with solve times on the order of 50 μs.**

***Index Terms*—Autonomous vehicles, human-in-the-loop, robust control, safety, vehicle safety, vehicle dynamics.**

I. Introduction

CONTROL systems capable of utilizing the entire operating range of vehicles can expand the ability of safety systems to assist drivers in emergency situations. For example, electronic stability control typically precludes significant oversteer, making techniques used by skilled drivers on low-grip surfaces (snow, ice) and in drifting impossible. Yet, expert drivers can precisely control a vehicle despite being in a state of oversteer where the vehicle is open-loop unstable. Imbuing these capabilities in driver assistance systems could enhance driving safety in a broader range of scenarios.

One such approach that has drawn attention for ensuring safety is control barrier functions (CBFs), which can be combined with quadratic programming (QP) to yield computationally efficient, minimally invasive controllers [1]. In CBF-based approaches, safety is enforced through forward invariance of a set in state space, and when combined with control Lyapunov functions (CLFs), performance objectives can also be met [2], [3], [4], [5]. However, safety guarantees can only be established assuming the model sufficiently captures the true system's dynamics. Robust CBFs seek to address this by maintaining safety when the system is subject to a disturbance or uncertainty, and adaptive robust CBFs seek to reduce conservativeness online [6], [7], [8], [9], [10]. Robustification of higher order systems remains an open challenge, and approaches have been developed when the input and disturbance have the same relative degree [11]. The relative degree assumption can be relaxed as in [12], but the safety constraint may no longer be control affine, yet can still be amenable to a second-order cone program.

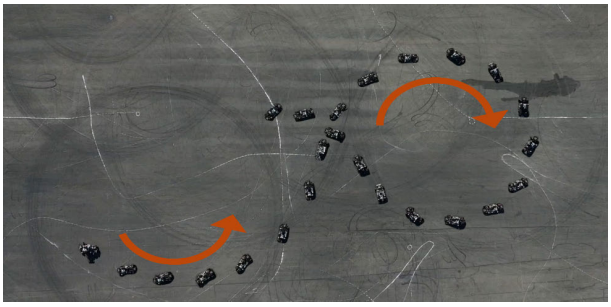


Fig. 1. Experimental validation of a figure eight maneuver with a CBF-based controller filtering driver commands.

When applying CBFs for automotive safety, adaptive cruise control (ACC), lane keeping [2], [3], [13], and emergency braking of connected automated vehicles (CAVs) [8] have all been explored. While these CBFs have been demonstrated for simple lateral and longitudinal driving scenarios, enforcing safety in coupled lateral and longitudinal dynamic scenarios, where the vehicle is operating at the handling limits and experiences strong nonlinearities, has yet to be established. Furthermore, these approaches do not explore the utility of CBFs for shared control of human-operated vehicles. For more complex coupled lateral and longitudinal control, nonlinear model predictive control (NMPC) has shown success in autonomous racing and drifting [14], [15], [16]. NMPC has been explored in a shared control setting where parallel autonomy was leveraged to amplify the driver's skills when racing and drifting [17], [18].

While these approaches have demonstrated the capability of controlling a vehicle in extreme situations, explicit safety guarantees are not considered, and NMPC is burdened by nonconvex optimization that can lead to high computational expense and local minima and infeasibility. Furthermore, the NMPC approaches do not provide formal forward invariance

Received 26 May 2026; accepted 22 July 2026. Date of publication 7 September 2026; date of current version 23 October 2026. Recommended by Associate Editor E. Lefeber. *(Corresponding author: James Dallas.)*

James Dallas, John Talbot, Makoto Suminaka, and John Subosits are with Toyota Research Institute, Los Altos, CA 94022 USA (e-mail: james.dallas@tri.global; john.talbot@tri.global; makoto.suminaka@tri.global; john.subosits@tri.global).

Illés Vörös and Gábor Orosz are with the University of Michigan, Ann Arbor, MI 48109 USA (e-mail: illesvoe@umich.edu; orosz@umich.edu).

Digital Object Identifier 10.1109/TCST.2026.3723769

1063-6536 © 2026 IEEE. All rights reserved, including rights for text and data mining, and training of artificial intelligence and similar technologies. Personal use is permitted, but republication/redistribution requires IEEE permission.
See https://www.ieee.org/publications/rights/index.html for more information.

guarantees analogous to those of CBFs. The CBF quadratic program (CBF-QP) approach pursued here provides formal safety guarantees through forward invariance while achieving computation times on the order of 50 μs, enabling real-time shared control.

In this work, we seek to address these aforementioned challenges through a CBF-based approach to prevent a vehicle from entering a state that would lead to unrecoverable motion. First, we present a robust adaptive higher order CBF (HOCBF) and a class of systems that yields a control affine constraint that can be integrated into a quadratic program. The maximal phase recoverable ellipse (MPREl) is developed as a smooth subset of the maximal phase recoverable envelope discussed in [19], acting as a safe set in the yaw rate–sideslip angle phase plane while also yielding a closed-form, analytical solution. Next, the robust adaptive CBF-based approach is placed on the MPREl, and a quadratic program ensures minimal intervention with driver inputs. The approach is validated with full-scale shared control drifting experiments highlighting the utility of the MPREl and robust adaptive CBF; see Fig. 1. Thus the original contributions are as follows.

1) A class of systems for robust adaptive HOCBFs is presented which remains control affine and amenable to QP.
2) The MPREl is presented as a safe subset to prevent unrecoverable motion and retain a closed-form, analytical solution.
3) A CBF-based approach to preventing a vehicle from entering the unrecoverable part of the state space is presented and validated in full-scale drifting experiments.

This work extends upon the conference proceedings in [20]. While the conference proceedings discussed the MPREl and exponential CBF (ECBF) formulation, this work extends the work to account for dynamic uncertainty. In particular, this article: 1) presents a higher order robust adaptive CBF that remains control affine; 2) extends the approach in [20] to a robust adaptive CBF-based approach; and 3) performs simulation and experimental validation to compare the nominal CBF of [20], a robust CBF-based approach, and an adaptive robust CBF-based approach for shared control drifting experiments with a tire-friction mismatch.

The rest of this article is structured as follows. Section II provides mathematical background on CBFs and states our main safety result. The vehicle dynamics, the maximum phase recoverable ellipse-based CBF design, and the quadratic program are introduced in Section III. The experimental platform is described in Section IV. The experimental validation with supporting numerical simulations is presented in Section V. Finally, concluding remarks are in Section VI.

II. Control Barrier Functions

A. Notation

$L_f h(x) = \nabla h(x) f(x)$ and $L_g h(x) = \nabla h(x) g(x)$ denote the Lie derivatives of function h along f and g. $\mathcal{N}$ denotes the null space of a matrix.

B. Background

Consider a system with control affine dynamics

$$\dot{x} = f(x) + g(x)u + \Delta(x) \tag{1}$$

with state $x \in \mathbb{X} \subset \mathbb{R}^n$, input $u \in \mathbb{U} \subset \mathbb{R}^m$, disturbance $\Delta \in \mathbb{R}^n$, and locally Lipschitz functions $f(x)$ and $g(x)$. For simplicity, we first provide background on enforcing safety for a known dynamical system, that is, for $\Delta = 0$.

Safety of a dynamical system is often defined by rendering a set forward invariant.

Definition 1 (Forward Invariance [1]): The set $\mathcal{S} \subset \mathbb{R}^n$ is forward invariant if $x(0) \in \mathcal{S} \Rightarrow x(t) \in \mathcal{S}\ \forall t \geq 0$ for the solutions of (1). Then we say that the set $\mathcal{S}$ is safe with respect to (1).

In particular, we seek to render the zero-superlevel set $\mathcal{S}$ of a continuously differentiable function $h : \mathbb{R}^n \to \mathbb{R}$ safe

$$\mathcal{S} = \{x \in \mathbb{R}^n : h(x) \geq 0\}. \tag{2}$$

Based upon this definition, enforcing nonnegativity of h establishes $\mathcal{S}$ as safe. More specifically, if $h(x(0)) \geq 0 \Rightarrow h(x(t)) \geq 0\ \forall t \geq 0$, then forward invariance of $\mathcal{S}$ is established. This motivates the notion of CBFs.

Definition 2 (CBF [1]): The continuously differentiable function $h : \mathbb{R}^n \to \mathbb{R}$ is a CBF for (1) on $\mathcal{S}$ defined by (2), if there exists $\alpha_0 > 0$ such that $\forall x \in \mathcal{S}$

$$\sup_{u \in \mathbb{R}^m} \left[\dot{h}(x,u)\right] = \sup_{u \in \mathbb{R}^m} \left[L_f h(x) + L_g h(x) u\right] > -\alpha_0 h(x) \tag{3}$$

where $L_f h(x)$ and $L_g h(x)$ are the Lie derivatives of h along f and g.

While Definition 2 leverages a linear function of h on the right-hand side, more generally any class-$\mathcal{K}$ function of h can be utilized. CBFs can then be utilized to establish a safe control law with the following theorem.

Theorem 1 [1]: If h is a CBF for (1) on $\mathcal{S}$ defined by (2), then any locally Lipschitz continuous controller $\xi : \mathbb{R}^n \to \mathbb{R}^m$, with $u = \xi(x)$ satisfying

$$\dot{h}(x,u) = L_f h(x) + L_g h(x) u \geq -\alpha_0 h(x) \tag{4}$$

$\forall x \in \mathcal{S}$ renders set $\mathcal{S}$ safe with respect to (1).

If $L_g h(x) \neq 0$, a minimally invasive quadratic program can be formulated to filter inputs in a safe manner by enforcing a constraint of the form (4). When $L_g h(x) = 0\ \forall x \in \mathbb{R}^n$, the notion of CBFs can be extended based on the relative degree of a system.

Definition 3: The k times continuously differentiable function $h : \mathbb{R}^n \to \mathbb{R}$ has an input relative degree (IRD) $k \geq 2$ for (1) if $\forall x \in \mathbb{R}^n$ we have $L_g h(x) = L_g L_f h(x) = \cdots = L_g L_f^{k-2} h(x) = 0$ and $L_g L_f^{k-1} h(x) \neq 0$.

For systems with dynamics (1) with IRD $k \geq 2$, an ECBF can be used to impose safety conditions [1], [21], [22]. Define the system

$$\begin{aligned} \dot{\eta}(x) &= F\eta(x) + G\mu \\ h(x) &= C\eta(x) \end{aligned} \tag{5}$$

where

$$F = \begin{bmatrix} 0 & 1 & 0 & \dots & 0 \\ 0 & 0 & 1 & \dots & 0 \\ \vdots & \vdots & \vdots & \ddots & \\ 0 & 0 & 0 & \dots & 1 \\ 0 & 0 & 0 & \dots & 0 \end{bmatrix}, \quad G = \begin{bmatrix} 0 \\ \vdots \\ 0 \\ 1 \end{bmatrix}$$

$$\eta(x) = \begin{bmatrix} h(x) \\ L_f(h(x)) \\ \vdots \\ L_f^{k-1}(h(x)) \end{bmatrix}, \quad C = \begin{bmatrix} 1 & 0 & \cdots & 0 \end{bmatrix} \tag{6}$$

and define the zero-superlevel sets $\mathcal{S}_i \subset \mathbb{R}^n$ of the functions $\nu_i(x) : \mathbb{R}^n \to \mathbb{R}$ as

$$\begin{aligned} &\nu_0(x) = h(x), && \mathcal{S}_0 = \{x \in \mathbb{R}^n : \nu_0(x) \geq 0\} \\ &\nu_1(x) = \dot{\nu}_0(x) + \alpha_0 \nu_0(x), && \mathcal{S}_1 = \{x \in \mathbb{R}^n : \nu_1(x) \geq 0\} \\ &\qquad\vdots \\ &\nu_{k-1}(x) = \dot{\nu}_{k-2}(x) + \alpha_{k-2}\nu_{k-2}(x) \\ &\qquad\qquad\qquad\qquad \mathcal{S}_{k-1} = \{x \in \mathbb{R}^n : \nu_{k-1}(x) \geq 0\} \end{aligned} \tag{7}$$

where $\mathcal{S}_0 = \mathcal{S}$ by definition. The roots of the characteristic polynomial of $F - G\Phi^\top$ define the scalars $-\alpha_i \in \mathbb{R}$, $i = 0, \ldots, k-1$ as

$$\begin{aligned} &(\lambda + \alpha_0)(\lambda + \alpha_1)\cdots(\lambda + \alpha_{k-1}) \\ &\quad = \lambda^k + \phi_{k-1}\lambda^{k-1} + \cdots + \phi_1\lambda + \phi_0 = 0 \end{aligned} \tag{8}$$

where the coefficients $\phi_i \in \mathbb{R}$, $i = 0, \ldots, k-1$ are used to compose the state feedback term

$$\mu = -\Phi^\top \eta(x), \quad \text{where} \quad \Phi^\top = \begin{bmatrix} \phi_0 & \phi_1 & \cdots & \phi_{k-1} \end{bmatrix}. \tag{9}$$

The previous construction is used to define an ECBF.

Definition 4 (ECBF [1]): Given a set $\mathcal{S} \subset \mathbb{R}^n$ defined as the zero-superlevel set of a k times continuously differentiable function $h : \mathbb{R}^n \to \mathbb{R}$, then h is an ECBF if there exists $\Phi \in \mathbb{R}^k$ such that $\forall x \in \text{Int}(\mathcal{S})$

$$\sup_{u \in \mathbb{R}^m} \left[L_f^k h(x) + L_g L_f^{k-1} h(x)\, u \right] > -\Phi^\top \eta(x) \tag{10}$$

which results in $h(x(t)) \geq Ce^{(F - G\Phi^\top)t}\eta(x(0)) \geq 0$ whenever $h(x(0)) \geq 0$.

Selecting the gain matrix Φ to ensure a valid ECBF of Definition 4 can be established through the following theorem.

Theorem 2 ([1], [21]): Suppose $\Phi \in \mathbb{R}^k$ is chosen such that the control system $F - G\Phi^\top$ has negative real eigenvalues which satisfy $-\alpha_i \leq \dot{\nu}_i(x(0))/\nu_i(x(0))$ for $i = 0, \ldots, k-1$. Then, $\mu = -\Phi^\top \eta(x)$ guarantees that $h(x)$ is an ECBF.

Finally, forward invariance of the set $\mathcal{S} \cap \mathcal{S}_1 \cap \cdots \cap \mathcal{S}_{k-1}$ can be established in Theorem 3.

Theorem 3: If h is a ECBF for (1) with sets $\mathcal{S}_i$, $i = 0, \ldots, k-1$ defined by (7), then any locally Lipschitz continuous controller $\psi : \mathbb{R}^n \to \mathbb{R}^m$, with $u = \psi(x)$ satisfying

$$L_f^k h(x) + L_g L_f^{k-1} h(x)\, u \geq -\Phi \eta(x) \tag{11}$$

$\forall x \in \mathcal{S}_{k-1}$ renders set $\mathcal{S} \cap \mathcal{S}_1 \cdots \cap \mathcal{S}_{k-1}$ safe with respect to (1).

Proof: If a controller satisfies the condition (11) then it renders S_{k-1} forward invariant according to Theorem 2. Then, following the argument in [23, Corollaries 1 and 2], $S_{k-2} \cap S_{k-1}$ is forward invariant. Using the same logic yields that $S_{k-3} \cap S_{k-2} \cap S_{k-1}$ is forward invariant and applying this approach successively yields the forward invariance of $\mathcal{S} \cap \mathcal{S}_1 \cap \cdots \cap \mathcal{S}_{k-1}$. ∎

C. Uncertainty Estimator

For this work, the uncertainty estimator of [12] is leveraged. The structure of the estimator and relevant properties are overviewed briefly, and the reader is referred to [12] for further details. Consider the uncertainty estimator expressed as

$$\begin{aligned} \hat{\Delta}(x, \rho) &= \Lambda x - \rho \\ \dot{\rho} &= \Lambda \left(f(x) + g(x)\, u + \hat{\Delta}(x, \rho) \right) \end{aligned} \tag{12}$$

where $\hat{\Delta} : \mathbb{X} \times \mathbb{R}^n \to \mathbb{R}^n$ is the estimated uncertainty, $\rho \in \mathbb{R}^n$ defines the auxiliary dynamics, and $\Lambda \in \mathbb{R}^{n \times n}$ is a diagonal positive definite matrix. The estimation error is expressed as

$$e(t) = \Delta(x(t)) - \hat{\Delta}(x(t), \rho(t)). \tag{13}$$

Assume that the uncertainty estimator is well-posed such that the following assumption holds.

Assumption 1 [12]: The uncertainty Δ and its derivative $\dot{\Delta}$ are bounded by $\delta_b > 0$ and $\delta_d > 0$, that is $\forall (x, u) \in \mathbb{X} \times \mathbb{U}$, $\|\Delta(x)\| \leq \delta_b, \|\dot{\Delta}(x, u)\| \leq \delta_d$.

Then the uncertainty estimator defined by (12) can be shown to be uniformly ultimately bounded through the following lemma.

Lemma 1 [12]: Consider the uncertain system (1) with a compound uncertainty function $\Delta : \mathbb{X} \to \mathbb{R}^n$ that satisfies Assumption 1 with upper bounds $\delta_b > 0$, $\delta_d > 0$, and the uncertainty estimator (12). Then e is uniformly ultimately bounded by

$$\bar{e}(t) = \delta_b \kappa e^{-\gamma t} + \delta_d \frac{\kappa}{\gamma}\left(1 - e^{-\gamma t}\right) \tag{14}$$

with

$$\kappa = \sqrt{\|P\| \left\|P^{-1}\right\|}, \quad \gamma = \frac{\lambda_{\min}(H)}{2\|P\|} \tag{15}$$

where $P \in \mathbb{R}^{n \times n}$ is the solution to the Lyapunov equation

$$-(\Lambda)^\top P + P(-\Lambda) + H = 0 \tag{16}$$

and Λ, $H \in \mathbb{R}^{n \times n}$ are design parameters with Λ representing the estimator gains of (12).

Remark 1: While the uncertainty bounds δ_b, δ_d may be explicitly determined for some systems, for more complex systems they can be obtained via a Monte Carlo study. In this work, the bounds are conservatively selected from simulation to ensure robustness across a range of operating conditions and fixed for all simulations and experiments.

D. Control Affine Robust HOCBFs

We are now ready to state the main result of this work that establishes a class of systems in which a robust HOCBF remains control affine. We remark that [12] proved forward invariance of robust HOCBFs under a constraint that is, in general, nonlinear in the input and only amenable to a second-order cone program. The main result of this work (Theorem 4), establishes a class of systems under which this exact constraint reduces to a control affine inequality, thus enabling a tractable quadratic program. First, suppose (1) satisfies the following assumption.

Assumption 2: Let system (1) be obtained through dynamic extension. That is, we express the state as $x = [\xi^\top, \sigma^\top]^\top \in \mathbb{R}^{n+m}$ and input as $u = \dot{\sigma} \in \mathbb{R}^m$. Furthermore, we assume

the disturbance enters through the same input channels as the original input σ.

Suppose the system is subject to disturbance $\Delta(x)$. The disturbance relative degree (DRD) is then defined as follows.

Definition 5: The k times continuously differentiable function $h : \mathbb{R}^{n+m} \to \mathbb{R}$ has a DRD k for (1) if $\forall x \in \mathbb{R}^{n+m}$ we have $L_\Delta h(x) = L_\Delta L_f h(x) = \cdots = L_\Delta L_f^{k-2} h(x) = 0$ and $L_\Delta L_f^{k-1} h(x) \neq 0$.

An HOCBF can be rendered safe under disturbance Δ as follows.

Theorem 4 (Main Result): Let h be an HOCBF defined on the state ξ for the uncertain system defined in (1) satisfying Assumption 2 with sets $\mathcal{S}_i$, $i = 0, \ldots, k-1$ defined by (7), and uncertainty satisfying Assumption 1. Furthermore, let $IRD = k$ and $DRD \geq k - 1$, and let $g(x)$ have full column rank, that is, its left pseudoinverse exists. Then any locally Lipschitz continuous controller $\psi : \mathbb{R}^{n+m} \to \mathbb{R}^m$, with $u = \psi(x)$ satisfying

$$\begin{aligned} &L_f \nu_{k-1}(x) + L_g \nu_{k-1}(x)\, u + \nabla \nu_{k-1}(x)\, \Delta + \Gamma(x)\, \dot{\Delta} \\ &\quad + (f(x) + g(x)\, u + \Delta)^\top \Theta(x)\, \Delta \\ &\geq -\alpha_{k-1}(\nu_{k-1}(x) + \Gamma(x)\, \Delta). \end{aligned} \tag{17}$$

$\forall x \in \tilde{\mathcal{S}}_{k-1}$ renders set $\mathcal{S} \cap \mathcal{S}_1 \cap \cdots \cap \tilde{\mathcal{S}}_{k-1}$ ($\tilde{\mathcal{S}}_{k-1} := \{x \in \mathbb{R}^{n+m} : \nu_{k-1}(x) + \Gamma(x)\Delta(x) \geq 0\}$) safe with respect to (1). Furthermore, constraint (17) reduces to the control affine sufficient condition (21).

Proof: The proof for forward invariance follows from [12, Th. 4]. To show that the constraint resulting from (17) remains control affine, from the bounds of Assumption 1 we have that $\|\dot{\Delta}\| \leq \delta_\mathrm{d}$ and $\|\Delta\| \leq \delta_\mathrm{b}$. Next, define $\Delta = \hat{\Delta} + e$ [see (13)] and $u = \bar{u} - g^\dagger(x)\hat{\Delta}$ as in [12], which decomposes the uncertainty into estimated uncertainty $\hat{\Delta}$ and estimation error e, and decomposes the input into nominal input $\bar{u}$ and the matched uncertainty $g^\dagger(x)\hat{\Delta}$, that enters the control channel. Substituting into (17), the bound may be obtained as

$$\begin{aligned} &L_f \nu_{k-1}(x) + L_g \nu_{k-1}(x)\left(\bar{u} - g^\dagger(x)\hat{\Delta}\right) + \nabla \nu_{k-1}(x)\hat{\Delta} \\ &\quad + \left(f(x) + g(x)\left(\bar{u} - g^\dagger(x)\hat{\Delta}\right) + \hat{\Delta}\right)^\top \Theta(x)\hat{\Delta} \\ &\quad - \left\| \left(f(x) + g(x)\left(\bar{u} - g^\dagger(x)\hat{\Delta}\right) + \hat{\Delta}\right)^\top \Theta(x) \right\| \bar{e} \\ &\quad - \|\Gamma(x)\| \delta_\mathrm{d} - \Omega(x, \bar{e}) \\ &\geq -\alpha_{k-1}\left(\nu_{k-1}(x) + \Gamma(x)\hat{\Delta} - \|\Gamma(x)\|\bar{e}\right) \end{aligned} \tag{18}$$

with

$$\Omega(x, \bar{e}) = \|\nabla \nu_{k-1}(x)\|\, \bar{e} + \|\Theta(x)\| \left\|\hat{\Delta}\right\| \bar{e} + \|\Theta(x)\|\, \bar{e}^2 \tag{19}$$

where the gradient $\Gamma : \mathbb{R}^{n+m} \to \mathbb{R}^{n+m}$ and the Hessian $\Theta : \mathbb{R}^{n+m} \to \mathbb{R}^{(n+m)\times(n+m)}$ are defined as

$$\Gamma(x) := \nabla\left(L_f^{k-2} h(x)\right), \quad \Theta(x) := \nabla^2\left(L_f^{k-2} h(x)\right). \tag{20}$$

Since $h(x) \triangleq h(\xi)$, $u = \dot{\sigma}$, and $IRD = k$, $\Theta(x)$ only contains elements corresponding to ξ, i.e., it is independent of terms related to σ. This results in $g(x)u \in \mathcal{N}(\Theta(x))$, that is, $(g(x)u)^\top \Theta(x) = 0$. Consequently, the terms containing $(f(x) + g(x)(\bar{u} - g^\dagger(x)\hat{\Delta}) + \hat{\Delta})^\top \Theta(x)$ become independent of the control input, simplifying (18) to

$$\begin{aligned} &L_f \nu_{k-1}(x) + L_g \nu_{k-1}(x)\left(\bar{u} - g^\dagger(x)\hat{\Delta}\right) + \nabla \nu_{k-1}(x)\hat{\Delta} \\ &\quad + \left(f(x) + \hat{\Delta}\right)^\top \Theta(x)\hat{\Delta} \\ &\quad - \left\| \left(f(x) + \hat{\Delta}\right)^\top \Theta(x) \right\| \bar{e} \\ &\quad - \|\Gamma(x)\| \delta_\mathrm{d} - \Omega(x, \bar{e}) \\ &\geq -\alpha_{k-1}\left(\nu_{k-1}(x) + \Gamma(x)\hat{\Delta} - \|\Gamma(x)\|\bar{e}\right) \end{aligned} \tag{21}$$

which is affine in the control input $\bar{u}$. ■

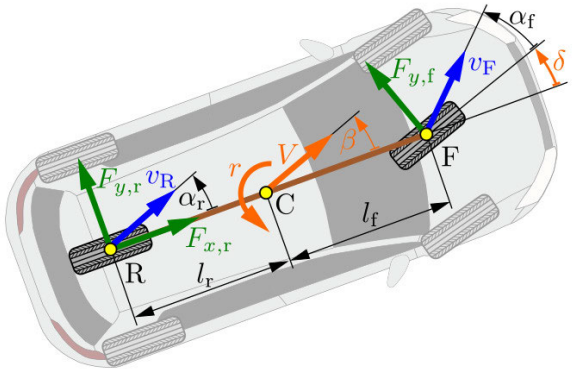


Fig. 2. Rear wheel drive single track vehicle model.

The usefulness of this result is that a quadratic program can be formulated for minimally invasive filtering, whereas the general result of [12] results in a second-order cone program. Our result applies to a general class of systems where the state is dynamically extended, and the uncertainty acts on the original states. Such systems are commonly encountered when input rates are treated as controls and the state consists of kinodynamic variables. Furthermore, (21) may be used to establish a robust CBF by holding $\bar{e}$ and $\hat{\Delta}$ constant or used in an adaptive robust CBF by updating $\bar{e}$ and $\hat{\Delta}$ with the estimator of Section II-C. In the next section, we demonstrate an application of this to prevent a vehicle from entering an unrecoverable state that would lead to a spinout.

Remark 2: The condition DRD $\geq$ IRD $-$ 1 requires that the disturbance enters the barrier function derivative chain no earlier than one step before the control input. In the vehicle model of Section III, $h(x)$ depends only on (r, β) (i.e., the yaw rate and the sideslip angle), and both input and disturbance enter through the force dynamics, yielding DRD = 1 and IRD = 2. More generally, this condition holds for systems satisfying Assumption 2 when the original system has IRD one with respect to σ, and the disturbance enters through the same channels as σ. Under this structure, dynamic extension $\dot{\sigma} = u$ shifts the control action one derivative later, so the IRD increases by one, while the DRD remains unchanged. This covers many kinodynamic systems where actuator rates serve as control inputs, common in vehicle, robotic, and aerospace applications. Furthermore, our vehicle has sufficiently fast actuation, enabling us to model actuator dynamics as an integrator as in Assumption 2.

III. Robust CBF for MPREL

A. Vehicle Dynamics

The proposed safety filter protects the vehicle from loss of control near its handling limits. It therefore requires a model which can accurately describe the vehicle's dynamic behavior in this regime. Many examples of high-performance driving from the literature show that the combination of a single-track vehicle model along with a modified Fiala brush tire model

performs well for limit driving tasks [15], [16], [24], [25]. The proposed safety filter operates solely on the vehicle's velocity states to ensure safety, namely the yaw rate r, the body sideslip angle β, and the speed V, all measured at the center of mass C, see Fig. 2. Extending the dynamic state of the system to include the roadwheel steering angle δ and the drive torque τ yields control affine dynamics in the form of (1). From this extension, the control inputs become steering rate $\dot{\delta}$ and drive torque rate $\dot{\tau}$. The complete state vector and input vector become $x = \begin{bmatrix} r & \beta & V & \delta & \tau \end{bmatrix}^\top$ and $\begin{bmatrix} \dot{\delta} & \dot{\tau} \end{bmatrix}^\top$, respectively. The control affine system dynamics are given by

$$f(x) = \begin{bmatrix} \frac{l_\mathrm{f}\left(F_{x,\mathrm{f}} \sin\delta + F_{y,\mathrm{f}} \cos\delta\right) - l_\mathrm{r} F_{y,\mathrm{r}}}{I_z} \\ \frac{F_{x,\mathrm{f}} \sin(\delta - \beta) + F_{y,\mathrm{f}} \cos(\delta - \beta) - F_{x,\mathrm{r}} \sin\beta + F_{y,\mathrm{r}} \cos\beta}{mV} - r \\ \frac{F_{x,\mathrm{f}} \cos(\delta - \beta) - F_{y,\mathrm{f}} \sin(\delta - \beta) + F_{x,\mathrm{r}} \cos\beta + F_{y,\mathrm{r}} \sin\beta}{m} \\ 0 \\ 0 \end{bmatrix}$$

$$g(x) = \begin{bmatrix} 0 & 0 & 0 & 1 & 0 \\ 0 & 0 & 0 & 0 & 1 \end{bmatrix}^\top \tag{22}$$

where l_f and l_r are the distances between the center of mass and front and rear axles, respectively, m is the mass of the vehicle, and I_z is the vehicle's mass moment of inertia about its center of mass C, see Fig. 2.

The tire model relates the slip angle of the tire (the angle between its velocity vector and longitudinal axis) to the lateral force it produces. Rigid body kinematics yield the slip angle of the front and rear tire given the velocity states of the vehicle

$$\begin{aligned} \alpha_\mathrm{f} &= \arctan\left(\frac{V\sin\beta + l_\mathrm{f} r}{V\cos\beta}\right) - \delta \\ \alpha_\mathrm{r} &= \arctan\left(\frac{V\sin\beta - l_\mathrm{r} r}{V\cos\beta}\right). \end{aligned} \tag{23}$$

A modified version of the Fiala brush tire model [24], [25], [26] captures the lateral forces generated as a function of its slip angle

$$F_y = \begin{cases} -C_\alpha \tan\alpha + \frac{C_\alpha^2}{3F_{y,\max}} |\tan\alpha| \tan\alpha \\ \qquad - \frac{C_\alpha^3}{27F_{y,\max}^2} \tan^3\alpha, & \text{if} \quad |\alpha| < \alpha_\mathrm{sl} \\ -F_{y,\max} \operatorname{sgn}\alpha, & \text{otherwise} \end{cases} \tag{24}$$

where C_α is the cornering stiffness, α_sl is the critical slip angle at which the tire reaches its friction limit, and $F_{y,\max}$ is the maximum lateral force. The critical slip angle is given by

$$\alpha_\mathrm{sl} = \operatorname{atan}\left(\frac{3F_{y,\max}}{C_\alpha}\right). \tag{25}$$

To capture the interaction of lateral and longitudinal forces near the tire's friction limits, we derate the maximum lateral force according to the applied longitudinal force as proposed in [25] and [27]

$$F_{y,\max} = \sqrt{(\mu F_z)^2 - \gamma F_x^2} \tag{26}$$

where μ is the coefficient of friction, F_z is the normal force, and $\gamma = 0.99$ acts as a tuning parameter to ensure numerical stability as the longitudinal force F_x reaches the tire's friction limit.

The normal forces on the front and rear tires are given by the static weight distribution of the vehicle

$$F_{z,\mathrm{f}} = \frac{mgl_\mathrm{r}}{l_\mathrm{f} + l_\mathrm{r}}, \quad F_{z,\mathrm{r}} = \frac{mgl_\mathrm{f}}{l_\mathrm{f} + l_\mathrm{r}}. \tag{27}$$

Assuming a rear wheel drive vehicle and ignoring wheel speed dynamics, the longitudinal forces become

$$F_{x,\mathrm{f}} = 0, \quad F_{x,\mathrm{r}} = \frac{\tau}{r_\mathrm{w}} \tag{28}$$

where τ is the wheel torque and r_w is the radius of the rear wheel.

B. MPREl Construction

In [20], a subset of the maximum phase recoverable envelope (MPRE), namely the MPREl, was presented as a candidate CBF to prevent a vehicle from entering an unrecoverable state. In areas beyond the set, control authority can be lost, and the vehicle may not be able to be stabilized, resulting in an unrecoverable spin [19]. The sideslip-yaw rate phase portrait corresponding to the inputs of $\delta = \pm\delta_{\max}$ and zero axle torque $\tau = 0$ provides a useful visualization of this set, as these inputs capture a large portion of recoverable states by effectively allocating tire force to balance the yaw moment [19]. Fig. 3 depicts the phase portrait for zero axle torque and negative and positive countersteer [Fig. 3(a) and (b), respectively], along with the MPREl (red).

The MPREl can be constructed leveraging the approach of [28], where a point on the beta nullcline ($\dot{\beta} = 0$) is used to establish a bounding contour such that a desired sideslip, $\beta = \pm\beta_{\max}$, is not exceeded. Considering that when both tires are saturated, $F_y = \mu F_z$, we can obtain r for the beta nullcline as

$$\begin{cases} r = \dfrac{\mu F_{z,\mathrm{f}} \cos\left(-\delta_{\max} - \beta_{\max}\right) + \mu F_{z,\mathrm{r}} \cos\beta_{\max}}{mV}, & \text{if } \delta \le 0 \\ r = \dfrac{-\mu F_{z,\mathrm{f}} \cos\left(\delta_{\max} - \beta_{\max}\right) - \mu F_{z,\mathrm{r}} \cos\beta_{\max}}{mV}, & \text{if } \delta \ge 0. \end{cases} \tag{29}$$

The dynamics can then be forward (purple) and reverse simulated (black) from the initial conditions of (29) to construct the bounding contours of Fig. 3. The MPREl is then obtained by fitting the largest ellipse in the bounding contours. Importantly, the MPREl is a subset of the MPRE, which is constructed at maximum steering authority, ensuring the resulting safe set respects the vehicle's input constraints by construction. If the boundary of the MPREl is violated momentarily, a stabilizing steering and torque action exists to drive the system back to the MPREl. While this construction could be used to update the ellipse parameters online, we fix the parameters for all simulations and experiments and allow the robust adaptive formulation to compensate for uncertainty.

C. MPREl Candidate-CBF

The MPREl is used to construct the candidate CBF in the form

$$h(x) = d - \left(a\beta^2 + b\beta r + cr^2\right) \tag{30}$$

with $a = 0.66$, $b = 0.0$, $c = 0.22$, and $d = 0.45$ being positive coefficients. This $h(x)$ is of relative degree 2 since $L_g h(x) = 0 \ \forall x \in \mathbb{R}^n$ but $L_g L_f h(x) \neq 0$. Thus, differentiation is needed for the control inputs to appear, and we can construct

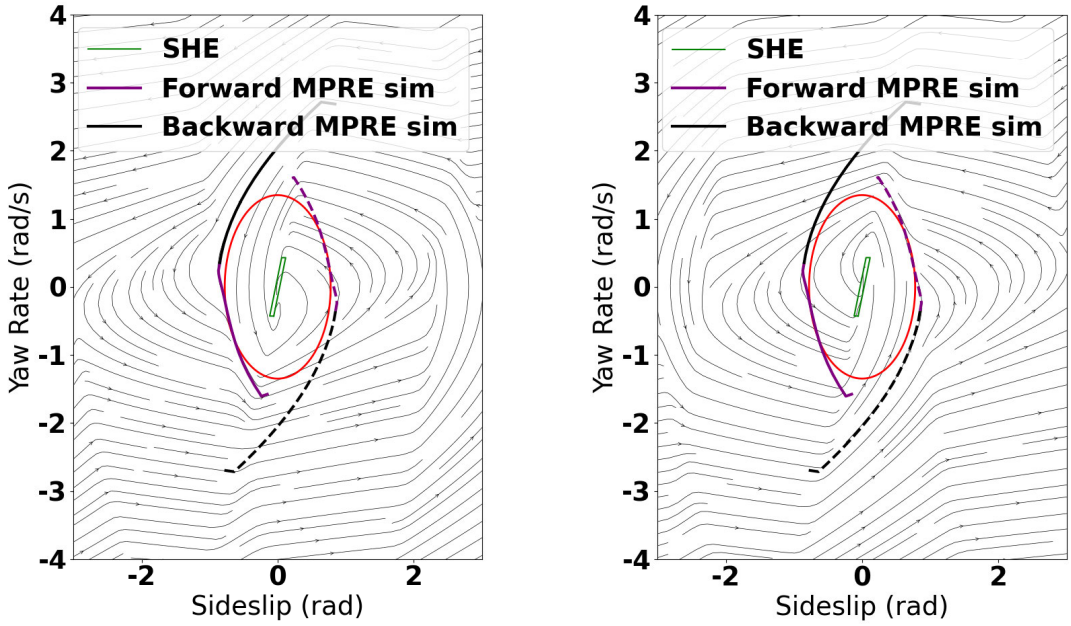


Fig. 3. Sideslip-yaw rate phase portrait. Trajectories are drawn at speed $V = 7\,\mathrm{m/s}$, no rear axle torque $\tau = 0$, and a steering angle of $\delta = \delta_{\max} = 0.71\,\mathrm{rad}$. Forward and reverse bounding trajectories are shown in purple and black, respectively. The MPREl is shown as the red ellipse, and the stable handling envelope (SHE), where the vehicle remains open-loop stable, is shown in green. (a) Negative steering. (b) Positive steering.

an ECBF as described in Section II. Taking the first derivative of (30) yields

$$L_f h(x) = -\left(2a\beta\dot{\beta} + b\dot{\beta}r + b\beta\dot{r} + 2cr\dot{r}\right) \tag{31}$$

with $\dot{\beta}$ and $\dot{r}$ defined in (22). Differentiating again yields the control inputs entering $\ddot{\beta}$ and $\ddot{r}$ expressed as

$$\begin{aligned} L_f^2 h(x) = -\big(&2a\dot{\beta}^2 + 2b\dot{\beta}\dot{r} + 2c\dot{r}^2 + \ddot{\beta}(2a\beta + br) \\ &+ \ddot{r}(b\beta + 2cr)\big). \end{aligned} \tag{32}$$

D. Minimally Invasive Quadratic Program

To achieve minimally invasive safety filtering, a CBF-QP is developed. Since the experimental vehicle interfaces through the steering angle δ and axle torque τ, the quadratic program is structured to match the driver's desired steering angle δ_{d} and desired axle torque τ_{d}. Then, the MPREl of Section III-C expresses the safe set. The quadratic program to filter the driver input with minimal intervention subject to the safety constraint of form (21) is thus given as

$$\begin{aligned} u_{\mathrm{QP}}(x) = \ &\underset{\bar{u}\in\mathbb{U}}{\arg\min}\ \frac{1}{2}(\bar{u} - u_{\mathrm{d}})^{\top} W (\bar{u} - u_{\mathrm{d}}) \\ &\text{s.t.}\quad L_f \nu_{k-1}(x) + L_g \nu_{k-1}(x)\left(\bar{u} - g^{\dagger}(x)\hat{\Delta}\right) \\ &\quad + \nabla \nu_{k-1}(x)\hat{\Delta} \\ &\quad + \left(f(x) + \hat{\Delta}\right)^{\top} \Theta(x)\hat{\Delta} \\ &\quad - \left\| \left(f(x) + \hat{\Delta}\right)^{\top} \Theta(x) \right\| \bar{e} \\ &\quad - \|\Gamma(x)\|\delta_{\mathrm{d}} - \Omega(x, \bar{e}) \\ &\quad \geq -\alpha_{k-1}\left(\nu_{k-1}(x) + \Gamma(x)\hat{\Delta} - \|\Gamma(x)\|\bar{e}\right) \end{aligned} \tag{33}$$

where W is a diagonal weighting matrix, $\bar{u} = \begin{bmatrix}\delta & \dot{\tau}\end{bmatrix}^{\top}$, u_{d} is the desired input, and $\Omega(x, \bar{e})$ is given by (19). Finite differences are used to convert between $[\,\delta_{\mathrm{QP}}\ \tau_{\mathrm{QP}}\,]$ and $[\,\dot{\delta}_{\mathrm{QP}}\ \dot{\tau}_{\mathrm{QP}}\,]$.



Fig. 4. Experimental platform.

The QP is solved through OSQP [29] and implemented with a slack variable to ensure numerical feasibility, although one may alternatively apply an analytical solution through the KKT conditions as in [30]. In addition, input constraints ($\mathbb{U} := \{u \mid u_{\min} \leq u \leq u_{\max}\}$) consistent with the vehicle capabilities are imposed.

IV. Experimental Platform

The experimental vehicle, shown in Fig. 4, is a custom-made drive-by-wire vehicle with dual-axle steering up to 0.71 rad at the front and rear axles. Each wheel is equipped with an in-hub Elaphe IWM M700 VD4 motor. Measurements are obtained at 200 Hz from a dual-antenna Oxford Technical Systems (OxTSs) RT3003 RTK-GPS/IMU system. Compute consists of a RAVE ATC8110-F and an Intel Xeon E-2278GE processor. All experiments are conducted on a large skidpad and were performed on a closed course.

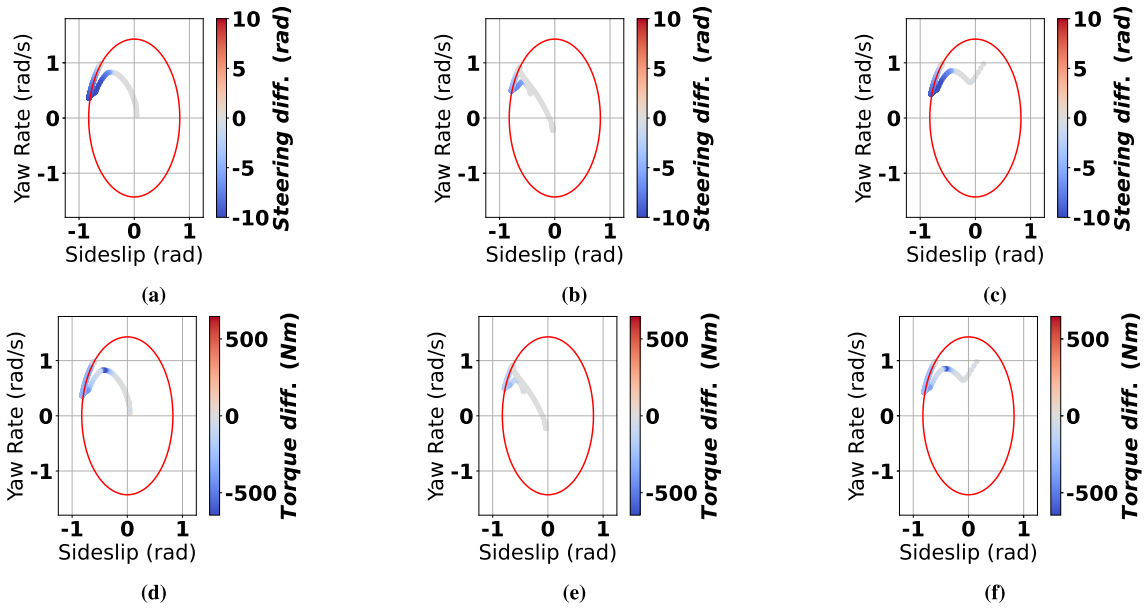


Fig. 5. Simulation phase plane intervention for various drifting segments. Intervention for the difference between filtered command and driver request for steering (top) and drive torque (bottom). (a) Drift initiation steering difference. (b) Drift equilibrium steering difference. (c) Drift transition steering difference. (d) Drift initiation torque difference. (e) Drift equilibrium torque difference. (f) Drift transition torque difference.

Dynamics emulation [31] is used to map driver inputs to a vehicle response corresponding to a low-friction surface. The emulated dynamics are obtained by applying the steering, accelerator, and brake inputs to a nonlinear single-track chassis model and a coupled slip Fiala tire model with tire-road friction of $\mu = 0.3$. The output of this model gives the desired chassis dynamics for the yaw rate, velocity, and sideslip. Then, dynamic inversion allocates the steering at each axle and individual brake and motor torques at each wheel such that the experimental vehicle achieves the desired chassis dynamics of the emulated model.

V. Results

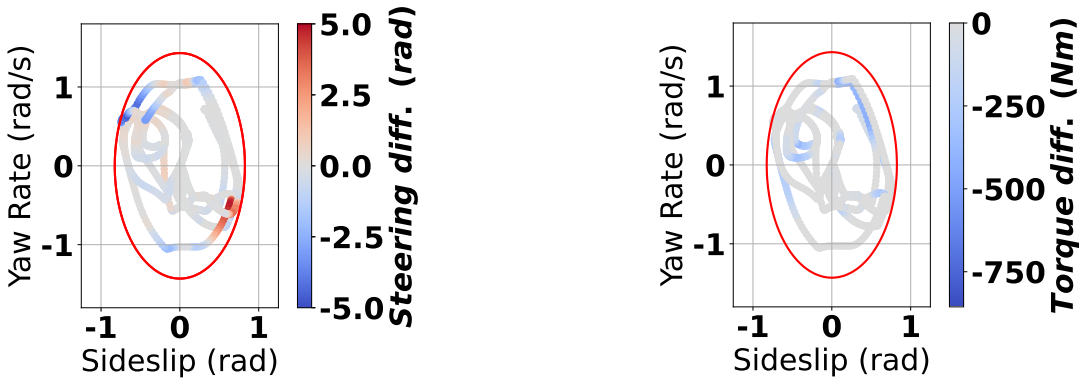
This section presents simulation and experimental results obtained from the platform described in Section IV. In all experiments, a human operator was driving the vehicle while attempting to drift, while the CBF-based controller filtered the driver commands in a minimally invasive manner. In Section V-A we present results when no uncertainty is present, highlighting the behavior of the CBF-based controller under nominal operating conditions. Then, in Section V-B, a friction mismatch between the CBF-based controller and the vehicle is induced to highlight the utility of the robust adaptive CBF-based controller.

A. Nominal Case

1) Simulation Results: To highlight the behavior of the CBF-QP of Section III-D in nominal conditions, simulations are performed with no uncertainty present between the control model and plant. Three cases are considered to depict different segments of drifting: 1) drift initiation; 2) a counterclockwise circular drift; and 3) a figure eight transition. These cases assess key aspects of drifting where: 1) assesses transitions from stable grip driving to sliding; 2) assesses drift stabilization; and 3) assesses transitions that are highly dynamic. For all three cases, the driver requests large throttle commands and reduced countersteer, as these inputs would lead to tire saturation and a loss of control. Results are demonstrated for counterclockwise drifting (positive yaw rate), and simulations performed for clockwise drifting (negative yaw rate) yielded a mirrored steering response but are omitted for brevity. In all discussion, inputs represent the rear axle torque and handwheel steering angle, where a linear map with a steering ratio of 1/15 converts between handwheel and roadwheel angle.

To assess transitioning from grip driving to sliding, a simulation where the vehicle starts with near zero yaw rate and sideslip is performed. For this case, the driver input request at the steering wheel and torque at the rear axle are 1.5 rad (measured at the handwheel) and 856 N · m, respectively. The intervention between the CBF-QP command and driver request is shown in Fig. 5(a) and (d), respectively. The intervention is shown by the color bar, where gray depicts the CBF matching the driver request, blue depicts the CBF decreasing the driver input, and red depicts an increase in driver input.

The CBF-QP initially matches the driver inputs, and the vehicle evolves in a counterclockwise loop toward the boundary (red ellipse). As the boundary is approached, the CBF-QP intervenes to prevent a spinout. At $\beta = -0.41$ rad the CBF-QP reduces both inputs, where the rear axle torque is reduced by a maximum of 678 N · m and the handwheel steering angle by −11.4 rad. Together, these inputs prevent a loss of control, as reducing the rear axle torque increases lateral tire force allocation and increasing countersteer increases lateral force at the front axle to balance the yaw moment. Once the vehicle begins to evolve in a safe manner along the boundary, the CBF-QP returns to matching the driver requests and stabilizes at $[\beta,\ r] = [-0.61\,\text{rad},\ 0.96\,\text{rad/s}]$. Finally, real-time performance is achieved with a mean solve time of 38.7 μs.



(a) (b)

Fig. 6. Experimental validation phase plane intervention (difference between filtered command and driver request) for (a) steering and (b) drive torque. Blue indicates the filter command reduced the driver request, while red indicates an increase.

In the next simulation, the vehicle is initialized at a drift equilibrium of $[\beta,\ r] = [-0.44\,\text{rad},\ 0.44\,\text{rad/s}]$. The equilibrium inputs are -4.5 rad at the handwheel and a rear axle torque of 364 N · m, and the driver requests -1.5 rad of handwheel steering angle and 700 N · m of rear axle torque. The CBF-QP intervention is shown in Fig. 5(b) and (e) for handwheel angle and rear axle torque, respectively.

The CBF-QP initially matches the driver input request as the vehicle evolves toward the boundary (red ellipse). To prevent a breach of the barrier, the CBF-QP deviates from the driver requests at $\beta = -0.73$ rad and reduces the torque by 272.6 N · m and steering by -10.3 rad at the handwheel. This causes the vehicle to generate larger stabilizing forces by maximally allocating the lateral force at the rear tire and balancing the yaw moment through increased countersteer at the front axle, preventing the vehicle from traversing over the barrier. As the vehicle evolves along the boundary, the CBF-QP begins to return to the driver request, and the vehicle eventually evolves back near the origin. Finally, the CBF-QP has a mean solve time of 40 μs.

The last simulation starts at $[\beta,\ r] = [0.15\,\text{rad},\ -0.98\,\text{rad/s}]$, corresponding to a segment of a transition from clockwise to counterclockwise drifting (i.e., a figure eight transition). The driver input requests are 1.5 rad of handwheel steering angle and 800 N · m of rear axle torque. The CBF-QP intervention is shown in Fig. 5(c) and (f). The vehicle evolves counterclockwise toward the safe set boundary (red ellipse), and the CBF-QP initially matches the driver requests. At $\beta = -0.38$ rad the CBF-QP intervenes and reduces the rear axle torque by 613 N · m and adjusts steering at the handwheel by -11 rad. This causes the vehicle to generate a larger stabilizing force by maximally allocating the lateral force at the rear tire and balancing the yaw moment through increased countersteer at the front axle, preventing the vehicle from traversing over the barrier. Finally, the CBF-QP has a mean solve time of 39.8 μs, achieving real-time performance.

2) Experimental Results: Experimental validation is performed for minimally invasive shared control on the platform described in Section IV. Fig. 1 shows an overhead view of a segment of the experiment where the driver is performing circular clockwise and counterclockwise drifts, and figure eight transitions. The CBF-QP intervention is shown for steering at the handwheel and axle torque in Fig. 6(a) and (b), respectively. The same notation and color map representation are used as shown in Fig. 5.

The vehicle trajectory follows counterclockwise evolution and can be divided into four quadrants. In quadrant I ($\beta > 0,\ r > 0$) the vehicle undergoes a figure eight transition from clockwise to counterclockwise drifting. In quadrant II ($\beta < 0,\ r > 0$) the vehicle is executing counterclockwise circular drifts. In quadrant III ($\beta < 0,\ r < 0$) the vehicle undergoes a figure eight transition from counterclockwise to clockwise drifts. Finally, in quadrant IV ($\beta > 0,\ r < 0$) clockwise circular drifts are performed.

The experiment provides a rich set of maneuvers highlighting different aspects of the CBF-QP behavior and covers a large portion of the phase portrait. Quadrant II contains small counterclockwise loops which represent the driver performing a stable counterclockwise drift. Minimal intervention occurs far from the boundary, as the driver applies safe commands that the CBF-QP accepts for steering [Fig. 6(a)] and torque [Fig. 6(b)]. Then the CBF-QP adjusts countersteer by -5.5 rad at the handwheel and reduces rear axle torque by 226 N · m as the vehicle approaches the boundary to prevent a breach of safety.

Transitions from counterclockwise to clockwise drifts (figure eight transition) are depicted by the large loops that start in quadrant II (counterclockwise drift), move through quadrant III and end in quadrant IV (clockwise drift). Successfully transitioning often requires a brief reduction in rear axle torque, along with a transition in countersteer from negative steering to the positive steering required to stabilize the clockwise drift. This torque reduction is observed in the CBF-QP intervention at $[\beta = -0.62\,\text{rad},\ r = -0.2\,\text{rad/s}]$ in Fig. 6(b), due to the driver requesting maximum torque. Then the CBF-QP gradually matches the driver torque request while guiding the driver in the transition from negative to positive steering. This steering transition is observed at $[\beta = 0.65\,\text{rad},\ r = -0.5\,\text{rad/s}]$ where the CBF-QP increases the steering angle by 5.1 rad, thereby aiding the driver in moving from a negative to positive steering angle.

A similar behavior is observed as the vehicle transitions from quadrant IV (clockwise drift) through quadrant I to quadrant II (counterclockwise drift). In particular, the CBF-QP

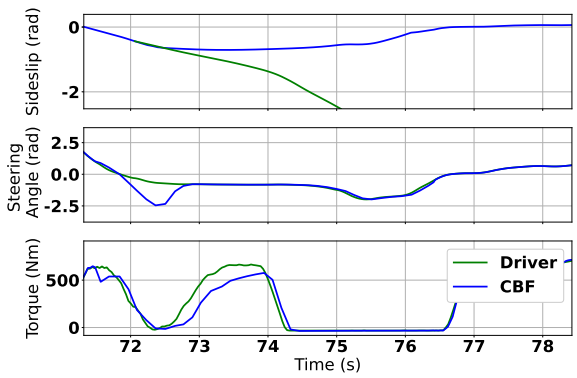


Fig. 7. Sideslip angle (top), steering angle (middle), and driving torque (bottom) experimental time trace. Commands realized after filtering with the CBF-QP are shown in blue, while driver request and simulated sideslip are in green. Baseline trajectory (green, top) loses stability and spins out.

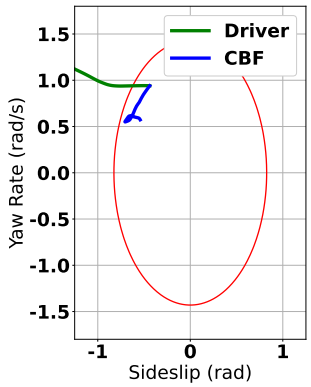


Fig. 8. Phase plane trajectory realized in experiment with CBF-QP filter (blue) and simulated response to driver inputs in the absence of intervention (green).

reduces torque by 407 N · m at [$\beta = 0.41$ rad, $r = 0.71$ rad/s], and then guides the steering by reducing steering by −5.5 rad at [$\beta = -0.65$ rad, $r = 0.6$ rad/s]. Together, these actions balance the yaw moment of the vehicle to prevent a loss of safety where the vehicle would otherwise traverse over the barrier in the upper left corner.

Demonstrating this intervention, Fig. 7 depicts a time trace of the figure eight transition with the driver input request (green) and CBF-QP command (blue) shown in the bottom two plots. The top plot shows the measured sideslip from the experiment when the CBF-QP filters the driver's commands (blue), while a forward simulation where the driver's commands have been directly applied is shown in green. The minimal intervention nature of the CBF-QP is highlighted, where the CBF-QP follows the driver's inputs in a safe manner by increasing and decreasing the steering angle and torque when the driver requests. This helps ensure the driver's inputs are safely followed, even if their commands are inherently unsafe, in this case performing a figure eight transition from positive to negative sideslip. Particularly as the vehicle transitions from positive to negative sideslip, from $t = 71$ to 74 s, the driver's rear axle torque request is reduced by 210 N · m (bottom) and additional countersteer is applied of −1.85 rad (middle). As shown by the measured sideslip (top), these actions stabilize the vehicle such that the sideslip does not exceed −0.71 rad.

On the other hand, posthoc analysis where forward simulations with the driver request applied directly to the single track model of Section III leads to a spiking sideslip indicating a spinout. Returning to the CBF-QP, once the drift is stabilized (74.4 s), the input commands return to respecting the driver request. Fig. 8 depicts this same scenario in the yaw rate–sideslip state space where the CBF-QP (blue) remains inside the safe set (red ellipse) while the posthoc simulation directly applying the driver inputs leads to a breach of safety (green). Thus, this demonstrates the utility of the proposed CBF-QP in real-world experiments.

B. Dynamic Uncertainty: Friction Mismatch

1) Simulation: Static Mismatch: Next, we analyze the CBF-QP behavior when dynamic uncertainty is present. In particular, simulations are performed where the simulation model is parameterized with a friction coefficient of 0.3 and the control model is parameterized with 33% higher friction of 0.4. Three cases are considered: 1) a nominal CBF-based control formulation parameterized with the friction mismatch but with no uncertainty compensation; 2) a robust CBF-based control formulation parameterized with the friction mismatch with conservative uncertainty compensation; and 3) the adaptive robust CBF-based control formulation initialized with the same parameters as the robust CBF-based control formulation but with online adaptation. For the estimator, we determine Λ and H to balance performance and safety from simulation and choose $\Lambda = \text{diag}(3.0\,\text{rad/s}, 3.0\,\text{m/s}, 3.0\,\text{rad})$, $H = \text{diag}(8.0, 8.0, 8.0)$, $\delta_b = 0.5$ and $\delta_d = 0.1$. For all cases, the driver input request is 1.5 rad of steering angle at the handwheel and 700 N · m of drive torque.

Fig. 9 depicts the difference in commanded input by the CBF-based controller and the driver request for handwheel angle (top) and drive torque (bottom). The nominal CBF-based controller formulation with no uncertainty compensation [Fig. 9(a) and (d)] struggles to converge due to infeasibility from model mismatch and lack of uncertainty compensation, leading to a breach of the barrier and vehicle spinout.

Adding in uncertainty compensation to the robust CBF-based controller prevents a spinout [Fig. 9(b) and (e)], but leads to conservativeness, achieving a peak sideslip of −0.4 rad. Peak intervention occurs at [β, r] = [−0.4 rad, 0.16 rad/s]. In particular, the steering is reduced by 6.7 rad at the handwheel, while drive torque is reduced by 325 N · m. These actions act to generate lateral forces at each axle that balance the yaw moment, preventing the yaw rate and sideslip from increasing to an unrecoverable state.

The adaptive CBF-based controller [Fig. 9(c) and (f)] prevents a spinout but with less conservativeness than the robust CBF-based controller, achieving a maximum sideslip of −0.55 rad. Peak intervention occurs at [β, r] = [−0.55 rad, 0.3 rad/s] with the steering reduced by 8.3 rad at the handwheel, and drive torque reduced by 766 N · m. The intervention for the adaptive CBF-based controller is considerably higher than the robust CBF-based controller as the vehicle reaches a point in the state space with higher sideslip and yaw rate, requiring more adjustment to stabilize the vehicle before entering an unrecoverable state.

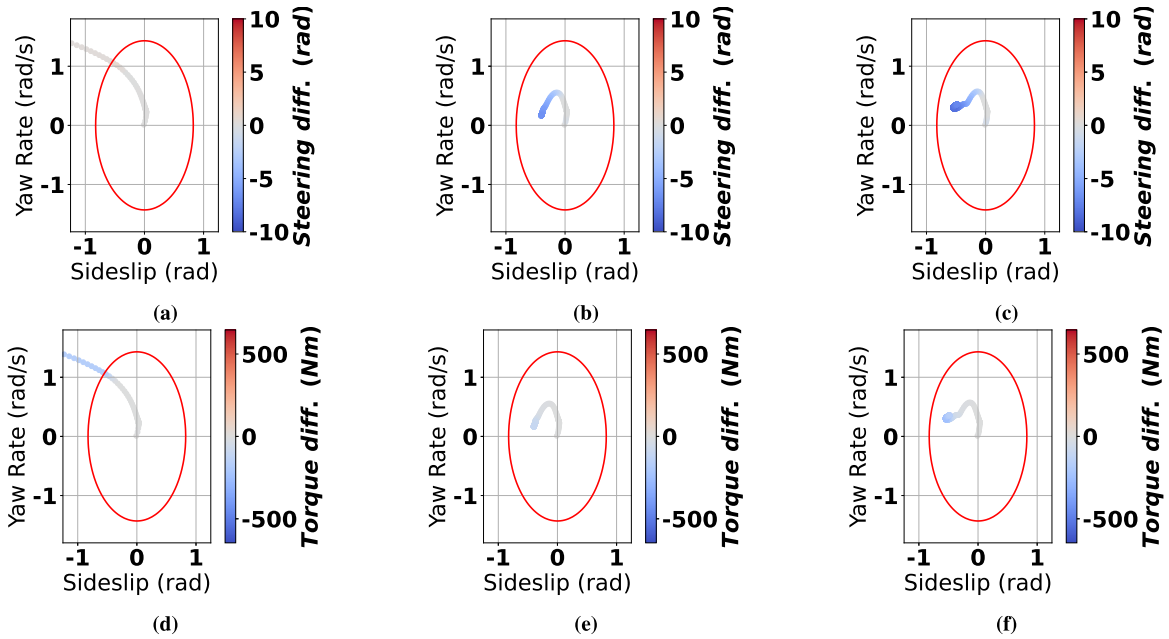


Fig. 9. Simulation phase portraits for the difference between CBF and driver steering angle (top), and driving torque (bottom). (a) Nominal CBF steering difference. (b) Robust CBF steering difference. (c) Adaptive CBF steering difference. (d) Nominal CBF torque difference. (e) Robust CBF torque difference. (f) Adaptive CBF torque difference.

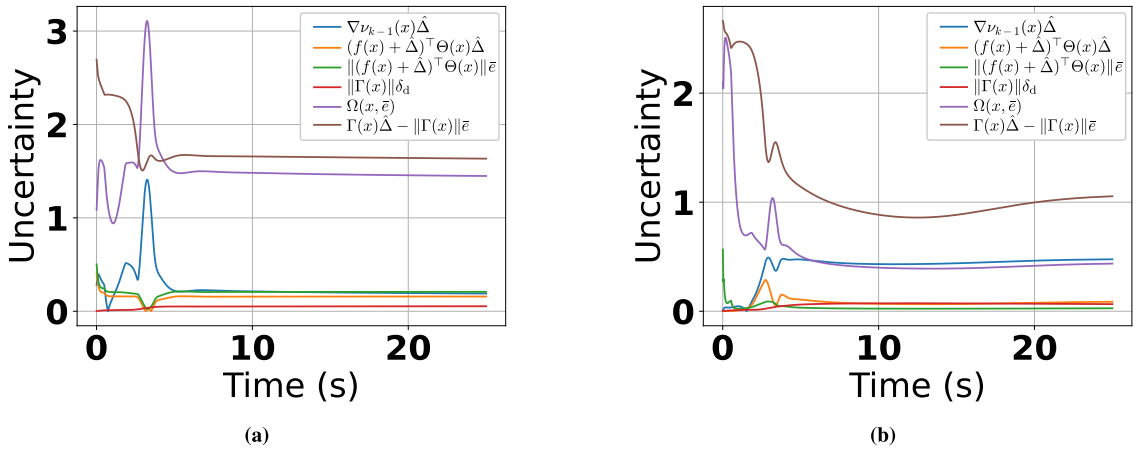


Fig. 10. Simulation results demonstrating uncertainty components for robust and adaptive CBF. (a) Uncertainty terms for robust CBF simulation. (b) Uncertainty terms for adaptive CBF simulation.

Fig. 10(a) and (b) depicts the magnitude of the uncertainty terms of the CBF constraint for $\nabla\nu_{k-1}(x)\hat{\Delta}$ (blue), $(f(x)+\hat{\Delta})^\top\Theta(x)\hat{\Delta}$ (orange), $\|(f(x)+\hat{\Delta})^\top\Theta(x)\|\bar{e}$ (green), $\|\Gamma(x)\|\delta_d$ (red), $\Omega(x,\bar{e})$ (purple), $\Gamma(x)\hat{\Delta}-\|\Gamma(x)\|\bar{e}$ (brown). Notably, the highest sensitivity is observed for $\nabla\nu_{k-1}(x)\hat{\Delta}$, $\Omega(x,\bar{e})$, and $\Gamma(x)\hat{\Delta}-\|\Gamma(x)\|\bar{e}$, while $(f(x)+\hat{\Delta})^\top\Theta(x)\hat{\Delta}$, $\|(f(x)+\hat{\Delta})^\top\Theta(x)\|\bar{e}$, and $\|\Gamma(x)\|\delta_d$ remain negligible. Thus, the terms with the highest sensitivity consist of the Lie derivative of ν_{k-1} along estimated uncertainty and estimation error $(\nabla\nu_{k-1}(x)\hat{\Delta}$ and $\Omega(x,\bar{e})$ which contains $\|\nabla\nu_{k-1}(x)\|\bar{e})$ and the impact of the uncertainties on the class-$\mathcal{K}$ function $(\Gamma(x)\hat{\Delta}-\|\Gamma(x)\|\bar{e})$. Furthermore, a reduction in the magnitude of the effect of the uncertainty on the CBF constraint is observed for the adaptive case [Fig. 10(b)] as compared to the robust case [Fig. 10(a)], allowing for a larger portion of the state space to be utilized.

2) Simulation: Time Varying Uncertainty: We further evaluate the adaptive robust CBF under a time-varying friction profile $\mu = 0.3 + 0.1\cos(2\pi t/10)$ which introduces continuous and significant variations in road conditions. In particular, based on the trajectory period $T = 2\pi/r$ with $r = 0.3$ rad/s [see Fig. 9(f)], one full circular motion ("donut") takes approximately 20 s, thus defining $\mu = 0.3 + 0.1\cos(2\pi t/10)$ yields friction changes representative of low adhesion every quarter revolution.

As shown in Fig. 11, despite this dynamic uncertainty, the system maintains stable behavior without violating safety constraints. At low-friction levels, the vehicle begins to enter a drift regime [Fig. 11(c)], at which point corrective steering intervention is applied to prevent loss of stability [Fig. 11(b)]. As friction increases, the vehicle progressively regains traction and returns toward the nominal trajectory under the nominal

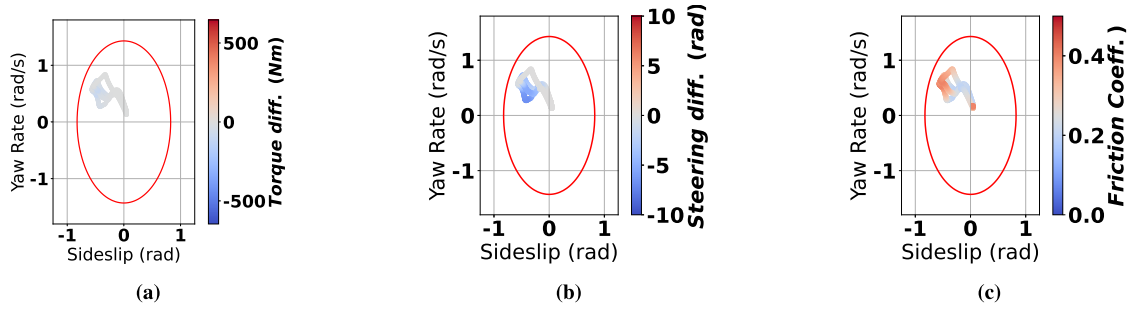


Fig. 11. Simulation phase plane intervention for time-varying friction. Intervention for the difference between filtered command and driver request for (a) drive torque, (b) steering, and (c) friction coefficient.

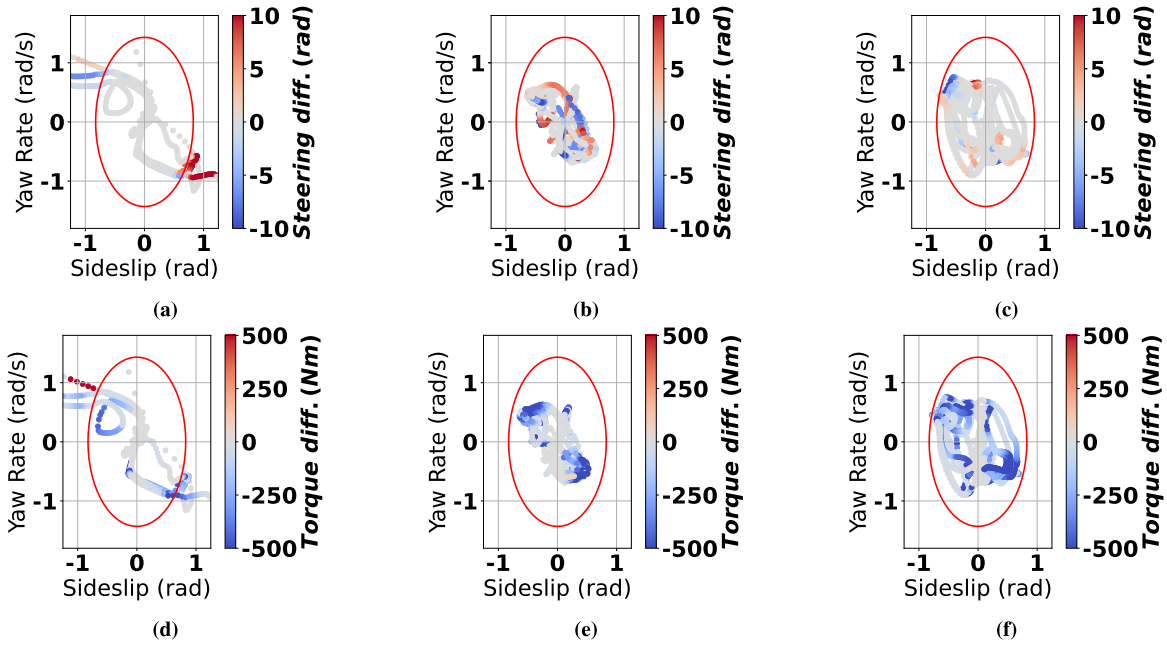


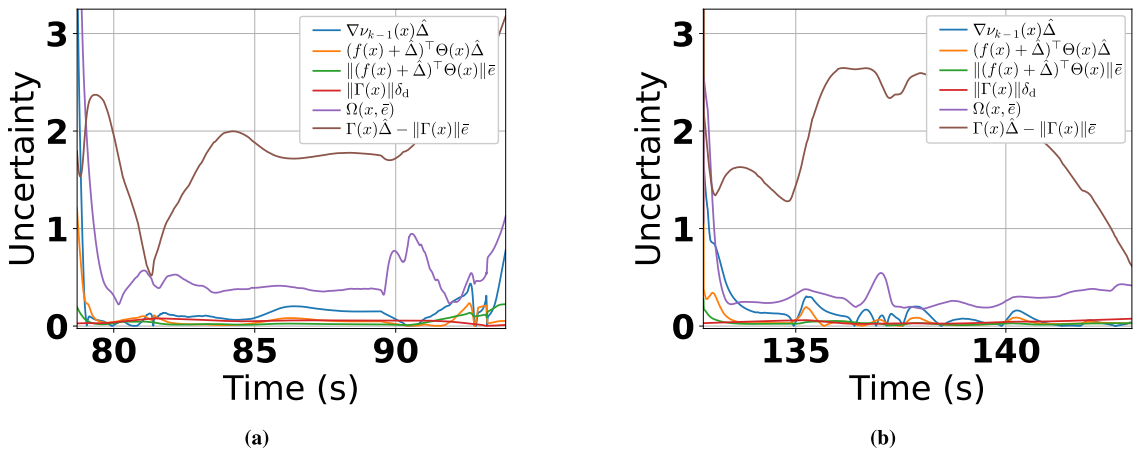
Fig. 12. Experimental phase portraits for the difference between CBF and driver steering angle (top), and driving torque (bottom). (a) Nominal CBF steering difference. (b) Robust CBF steering difference. (c) Adaptive CBF steering difference. (d) Nominal CBF torque difference. (e) Robust CBF torque difference. (f) Adaptive CBF torque difference.

driver inputs $\delta = 0.1$ rad, $\tau = 375$ N $\cdot$ m. These results demonstrate that the proposed controller maintains safety and performance under significant time-varying friction, validating its robustness to dynamic uncertainties.

Finally, we remark that while Theorem 4 establishes forward invariance for the exact constraint (33) without relaxation, the slack variable in the OSQP formulation acts primarily as a numerical safeguard and was not observed to impact safety in practice. Due to sufficiently fast actuation, the vehicle utilized at most 35% of its available control authority. The slack variable remains negligible throughout (on the order 10^{-5}) and is only activated due to numerical considerations rather than meaningful violations of the CBF constraint.

3) Experimental Validation: Next, experimental validation is performed on the vehicle described in Section IV. The driver is performing circular clockwise and counterclockwise drifts, and figure eight maneuvers. The same three cases are considered: 1) a nominal CBF-based control formulation parameterized with a friction mismatch but with no uncertainty compensation; 2) a robust CBF-based control formulation parameterized by the friction mismatch with conservative uncertainty compensation; and 3) the adaptive robust CBF-based control formulation initialized with the same parameters of the robust CBF-based control formulation but with online adaptation. For all cases, a 33% friction mismatch is assumed where the dynamics model (1) is parameterized with a friction coefficient of 0.4, while the plant has a friction coefficient of 0.3. This mismatch leads to the control model generating more stabilizing force than is available on the actual vehicle, leading to loss of control if not compensated for.

The experimental results are depicted in Fig. 12, showing the steering and engine torque intervention. Fig. 12(a) and (d) shows the case for the nominal CBF-based controller with no uncertainty compensation, which leads to barrier breaches where the vehicle loses control and spins out. Accounting for uncertainty with a robust CBF-based controller can maintain control of the vehicle and prevent spinouts, but yields conservative behavior. Fig. 12(b) and (e) depicts this, and while the vehicle can drift safely, a small subset of the state space is used where the peak magnitude of sideslip and yaw rate achieved are 0.64 rad and 0.7 rad/s. This conservativeness prevents smooth transitions between drifting



(a) (b)

Fig. 13. Experimental results demonstrating uncertainty components of sustained drift segment for robust and adaptive CBF. (a) Uncertainty terms for robust CBF experiment. (b) Uncertainty terms for adaptive CBF experiment.

in the counterclockwise and clockwise directions (i.e., figure eight transitions), ultimately causing the vehicle to regain traction and exit the drift by returning near the origin before reinitiating the drift in the opposite direction.

The adaptive robust CBF-based controller achieves safe behavior, preventing the vehicle from losing control and spinning out while recovering a large portion of the state space. Fig. 12(c) and (f) depicts this, where the vehicle achieves a peak magnitude for sideslip and yaw rate of 0.78 rad and 0.9 rad/s. Furthermore, by reducing conservativeness, the vehicle is able to smoothly transition between clockwise and counterclockwise drifts to successfully perform figure eight transitions without regaining traction as in the robust CBF-based controller. These results demonstrate the applicability of the approach to account for uncertainty in driver-in-the-loop experiments.

Fig. 13(a) and (b) depicts the magnitude of the uncertainty terms of the CBF constraint for $\nabla\nu_{k-1}(x)\hat{\Delta}$ (blue), $(f(x) + \hat{\Delta})^\top\Theta(x)\hat{\Delta}$ (orange), $\|(f(x) + \hat{\Delta})^\top\Theta(x)\|\bar{e}$ (green), $\|\Gamma(x)\|\delta_d$ (red), $\Omega(x,\bar{e})$ (purple), $\Gamma(x)\hat{\Delta} - \|\Gamma(x)\|\bar{e}$ (brown) for segments of the experiment where a drift was sustained. Similar to simulation, the highest sensitivity is observed for $\nabla\nu_{k-1}(x)\hat{\Delta}$, $\Omega(x,\bar{e})$, and $\Gamma(x)\hat{\Delta} - \|\Gamma(x)\|\bar{e}$, while $(f(x) + \hat{\Delta})^\top\Theta(x)\hat{\Delta}$, $\|(f(x) + \hat{\Delta})^\top\Theta(x)\|\bar{e}$, and $\|\Gamma(x)\|\delta_d$ remain negligible. It should be noted that due to variations in driver inputs, a direct comparison between the robust and adaptive disturbance is challenging, although a reduction in the magnitude of the effect of the uncertainty on the CBF constraint is observed for the adaptive case [Fig. 13(b) as compared to the robust case Fig. 13(a)], throughout the experiment.

VI. Conclusion

This article explored minimally invasive shared control to prevent a vehicle from losing control through ECBFs. In particular, we define the MPREl as a safe set in the sideslip angle–yaw rate phase plane that prevents a loss of control. We then present a class of systems that allows higher order adaptive robust CBFs to remain control affine and thus be formulated in a quadratic program. Simulations and experiments validate the MPREl for shared control of a drifting vehicle when no uncertainty is present. We then highlight the ability of the adaptive robust HOCBF to maintain safety under a friction mismatch between the plant and control model through simulation and experiments of a drifting vehicle, extending the practical utility of the approach. The results show that the formulation follows the driver's intentions if safe, and adjusts steering and throttle to stabilize the vehicle if necessary. Finally, the proposed approach achieves a computation time of less than 50 μs, demonstrating real-time performance. Future work could investigate actuator constraints; however, we found the vehicle had sufficient actuation to achieve good practical performance.

References

[1] A. D. Ames, S. Coogan, M. Egerstedt, G. Notomista, K. Sreenath, and P. Tabuada, "Control barrier functions: Theory and applications," in *Proc. IEEE 18th Eur. Control Conf.* (ECC), 2019, pp. 3420–3431.

[2] X. Xu, P. Tabuada, J. W. Grizzle, and A. D. Ames, "Robustness of control barrier functions for safety critical control," *IFAC-PapersOnLine*, vol. 48, no. 27, pp. 54–61, 2015.

[3] A. D. Ames, X. Xu, J. W. Grizzle, and P. Tabuada, "Control barrier function based quadratic programs for safety critical systems," *IEEE Trans. Autom. Control*, vol. 62, no. 8, pp. 3861–3876, Aug. 2017.

[4] J. Breeden and D. Panagou, "Compositions of multiple control barrier functions under input constraints," in *Proc. Amer. Control Conf.*, 2023, pp. 3688–3695.

[5] J. Zeng, B. Zhang, and K. Sreenath, "Safety-critical model predictive control with discrete-time control barrier function," in *Proc. IEEE Amer. Control Conf. (ACC)*, 2021, pp. 3882–3889.

[6] M. Jankovic, "Robust control barrier functions for constrained stabilization of nonlinear systems," *Automatica*, vol. 96, pp. 359–367, Oct. 2018.

[7] A. Alan, T. G. Molnar, A. D. Ames, and G. Orosz, "Parameterized barrier functions to guarantee safety under uncertainty," *IEEE Control Syst. Lett.*, vol. 7, pp. 2077–2082, 2023.

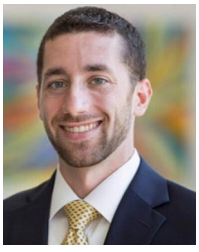
[8] A. Alan, A. J. Taylor, C. R. He, A. D. Ames, and G. Orosz, "Control barrier functions and input-to-state safety with application to automated vehicles," *IEEE Trans. Control Syst. Technol.*, vol. 31, no. 6, pp. 2744–2759, Nov. 2023.

[9] J. Breeden and D. Panagou, "Robust control barrier functions under high relative degree and input constraints for satellite trajectories," *Automatica*, vol. 155, Sep. 2023, Art. no. 111109.

[10] A. Alan, T. G. Molnar, A. D. Ames, and G. Orosz, "Generalizing robust control barrier functions from a controller design perspective," *IEEE Open J. Control Syst.*, vol. 4, pp. 54–69, 2025.

[11] M. H. Cohen and C. Belta, "High order robust adaptive control barrier functions and exponentially stabilizing adaptive control Lyapunov functions," in *Proc. IEEE Amer. Control Conf.*, 2022, pp. 2233–2238.

[12] E. Daş and J. W. Burdick, "Robust control barrier functions using uncertainty estimation with application to mobile robots," *IEEE Trans. Autom. Control*, vol. 70, no. 7, pp. 4766–4773, Jul. 2025.
[13] C. Jiang, H. Gan, I. Vörös, D. Takács, and G. Orosz, "Safety filter for lane-keeping control," in *Proc. 16th Int. Symp. Adv. Vehicle Control*, 2024, pp. 1–6.
[14] M. Thompson, J. Dallas, J. Y. M. Goh, and A. Balachandran, "Adaptive nonlinear model predictive control: Maximizing tire force and obstacle avoidance in autonomous vehicles," *IEEE Trans. Field Robot.*, vol. 1, pp. 318–331, 2024.
[15] V. Laurense, "Integrated motion planning and control for automated vehicles up to the limits of handling," *Ph.D. dissertation, Dept. Mech. Eng., Stanford University*, Stanford, CA, USA, 2019.
[16] J. Y. M. Goh, M. Thompson, J. Dallas, and A. Balachandran, "Beyond the stable handling limits: Nonlinear model predictive control for highly transient autonomous drifting," *Vehicle Syst. Dyn.*, vol. 62, no. 10, pp. 1–24, Oct. 2024.
[17] J. Talbot, M. Brown, and J. C. Gerdes, "Shared control up to the limits of vehicle handling," *IEEE Trans. Intell. Vehicles*, vol. 9, no. 1, pp. 2977–2987, Jan. 2024.
[18] I. Karino, J. Dallas, and Y. M. Jonathan Goh, "Shared control for giving ordinary drivers expert level drifting skills," in *Proc. IEEE Int. Conf. Syst., Man, Cybern. (SMC)*, Oct. 2023, pp. 1461–1467.
[19] J. Y. M. Goh, *Automated Vehicle Control Beyond Stability Limits*. Stanford, CA, USA: Stanford Univ. Press, 2019.
[20] J. Dallas et al., "Control barrier functions for shared control and vehicle safety," in *Proc. Amer. Control Conf. (ACC)*, Jul. 2025, pp. 4203–4210.
[21] Q. Nguyen and K. Sreenath, "Exponential control barrier functions for enforcing high relative-degree safety-critical constraints," in *Proc. Amer. Control Conf. (ACC)*, 2016, pp. 322–328.
[22] W. Xiao, C. G. Cassandras, and C. A. Belta, "Bridging the gap between optimal trajectory planning and safety-critical control with applications to autonomous vehicles," *Automatica*, vol. 129, Jul. 2021, Art. no. 109592.
[23] T. G. Molnar, G. Orosz, and A. D. Ames, "On the safety of connected cruise control: Analysis and synthesis with control barrier functions," in *Proc. 62nd IEEE Conf. Decis. Control (CDC)*, Dec. 2023, pp. 1106–1111.
[24] E. Fiala, "Seitenkräfte am rollenden luftreifen (Lateral forces on the rolling pneumatic tire)," *Zeitschrift der Vereines Deutscher Ingenieure (Magazine Assoc. German Engineers)*, vol. 96, pp. 973–979, Oct. 1954.
[25] I. Vörös, D. Takács, and G. Orosz, "Cornering with driving torque: Steady state cornering, donuts, drifting," in *Proc. 29th IAVSD Int. Symp. Dyn. Vehicles Roads Tracks*, 2025.
[26] H. Pacejka, *Tire and Vehicle Dynamics*. Amsterdam, The Netherlands: Elsevier, 2005.
[27] R. Y. Hindiyeh and J. C. Gerdes, "Design of a dynamic surface controller for vehicle sideslip angle during autonomous drifting," *IFAC Proc. Volumes*, vol. 43, no. 7, pp. 560–565, Jul. 2010.
[28] J. Dallas et al., "Safe stability envelopes and shared control for active vehicle safety," in *Proc. IEEE Conf. Control Technol. Appl. (CCTA)*, Aug. 2024, pp. 561–568.
[29] B. Stellato, G. Banjac, P. Goulart, A. Bemporad, and S. Boyd, "OSQP: An operator splitting solver for quadratic programs," *Math. Program. Comput.*, vol. 12, no. 4, pp. 637–672, Dec. 2020.
[30] T. G. Molnar, S. K. Kannan, J. Cunningham, K. Dunlap, K. L. Hobbs, and A. D. Ames, "Collision avoidance and geofencing for fixed-wing aircraft with control barrier functions," *IEEE Trans. Control Syst. Technol.*, vol. 33, no. 5, pp. 1493–1508, Sep. 2025.
[31] H. E. B. Russell and J. C. Gerdes, "Design of variable vehicle handling characteristics using four-wheel steer-by-wire," *IEEE Trans. Control Syst. Technol.*, vol. 24, no. 5, pp. 1529–1540, Sep. 2016.



James Dallas received the B.S. degree in mechanical engineering from Pennsylvania State University, University Park, PA, USA, in 2017, and the M.S. and Ph.D. degrees in mechanical engineering from the University of Michigan, Ann Arbor, MI, USA, in 2018 and 2021, respectively.

He is currently a Senior Research Scientist with Toyota Research Institute, Los Altos, CA, USA. His research interests include modeling, system identification, system dynamics and control, shared control, and adaptive and robust optimal control, with applications to vehicle systems.



John Talbot (Member, IEEE) received the B.M.E. degree from Auburn University, Auburn, AL, USA, in 2016, and the M.S. and Ph.D. degrees from Stanford University, Stanford, CA, USA, in 2019 and 2024, respectively.

He currently works as a Research Scientist with Toyota Research Institute, Los Altos, CA, USA. His research interests include vehicle dynamics and optimal control applied to advanced driver assistance systems and automotive safety.



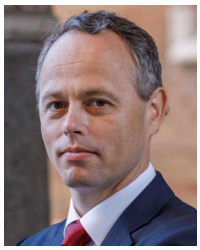
Makoto Suminaka received the B.S. and M.S. degrees in mechanical engineering from The University of Osaka, Osaka, Japan, in 2014 and 2016, respectively.

He is currently a Senior Engineer with Toyota Research Institute, Los Altos, CA, USA. His research interests include model predictive control, control barrier functions, adaptive and learning-based control, and their applications to vehicle dynamics and autonomous driving.



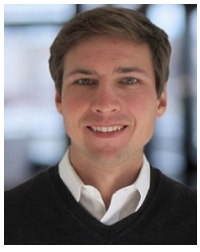
Illés Vörös received the B.S. degree in mechatronics engineering and the M.S. and Ph.D. degrees in mechanical engineering from Budapest University of Technology and Economics, Budapest, Hungary, in 2016, 2019, and 2024, respectively.

He is currently working as a Post-Doctoral Researcher at the University of Michigan, Ann Arbor, MI, USA. His research interests include time delay systems, nonlinear dynamics, and control with application to automated vehicles.



Gábor Orosz (Senior Member, IEEE) received the M.Sc. degree in engineering physics from Budapest University of Technology and Economics, Budapest, Hungary, in 2002, and the Ph.D. degree in engineering mathematics from the University of Bristol, Bristol, U.K., in 2006.

He is currently a Professor of mechanical engineering and a Professor of civil and environmental engineering at the University of Michigan, Ann Arbor, MI, USA. His research interests include nonlinear dynamics and control, time delay systems, machine learning, and data-driven systems with applications to connected and automated vehicles, traffic flow, and biological networks.



John Subosits received the B.S.E. degree in mechanical and aerospace engineering from Princeton University, Princeton, NJ, USA, in 2013, and the M.S. and Ph.D. degrees in mechanical engineering from Stanford University, Stanford, CA, USA, in 2015 and 2020, respectively.

He currently leads the Extreme Performance Intelligent Control Group, Toyota Research Institute (TRI), Los Altos, CA, USA. His research interests include algorithms for vehicle control that match the performance, robustness, and adaptability of the best human (racing) drivers.